3D CT-Video Fusion for Image-Guided Bronchoscopy

William E. Higgins,[1,*] James P. Helferty,[1,2] Kongkuo Lu,[1] Scott A. Merritt,[1] Lav Rai,[1] and Kun-Chang Yu[1]

[1]Depts. of Electrical Engineering and Computer Science and Engineering,
Penn State University, University Park, PA 16802

[2]MilSys Technologies, Bridgeport, PA 19405

[*]Corresponding author. Fax: 1-814-863-5341. Email address: weh2@psu.edu

Abstract

Bronchoscopic biopsy of the central-chest lymph nodes is an important step for lung-cancer staging. Before bronchoscopy, the physician first visually assesses a patient's three-dimensional (3D) computed tomography (CT) chest scan to identify suspect lymph-node sites. Next, during bronchoscopy, the physician guides the bronchoscope to each desired lymph-node site. Unfortunately, the physician has no link between the 3D CT image data and the live video stream provided during bronchoscopy. Thus, the physician must essentially perform biopsy blindly, and the skill levels between different physicians differ greatly. We describe an approach that enables synergistic fusion between the 3D CT data and the bronchoscopic video. Both the integrated planning and guidance system and the internal CT-video registration and fusion methods are described. Phantom, animal, and human studies illustrate the efficacy of the methods.

Keywords: virtual endoscopy, virtual bronchoscopy, image-guided surgery, image fusion, lung cancer

1 INTRODUCTION

Interventional biopsy of the central-chest lymph nodes is an important step for staging lung cancer [1]. Trans-bronchial needle aspiration (TBNA) is often used to sample lymph nodes for pathology [2–5]. To perform TBNA, the physician first visually assesses a patient's computed tomography (CT) scan to identify suspect lymph-node sites. Later, during subsequent live bronchoscopy, the physician guides the bronchoscope to each desired lymph-node site.

The physician must use prior experience and the available 3D CT chest data to do this guidance. This requires the physician to do 3D mental reconstruction of the anatomy to ascertain each biopsy site. CT, however, only provides transverse-plane (x-y) sections of the chest anatomy, and it is well-known that physicians have difficulty properly identifying airways in CT data by as early as the second generation [6,7]. Thus, effective bronchoscopy path planning can be difficult. Further, the target lymph nodes are behind airway walls and hidden from the bronchoscope's field of view. It has been shown that the act of positioning the biopsy needle is extremely stressful to the bronchoscopist and that the skill level of bronchoscopists varies significantly [8]. Overall, this results in low biopsy yields [3].

The development of *virtual bronchoscopy* (VB) has led to interest in introducing CT-based computer-graphics techniques into the procedure of lung-cancer staging [9–14]. In VB, the 3D

CT image serves as a high-resolution digital-image replica of the chest. Interior (endoluminal) renderings of the airways can be generated along paths following the airway central axes and lead to an off-line simulation of live videobronchoscopy. VB is a subspecialty of the general field referred to as *virtual endoscopy* [15, 16]. In virtual endoscopy, interior views of organs are computer-generated from radiologic images. This is similar to the situation where interior video views of organs are presented during real endoscopy.

VB has inspired proposals where computer-based image guidance assists the physician in performing TBNA. These proposals, summarized below, show promise, but can be improved upon: (1) McAdams *et al.* and Hopper *et al.* applied 3D CT-based analysis (virtual bronchoscopy) to lymph-node biopsy, but these efforts involved no live guidance [3, 4]; (2) Bricault *et al.* did rudimentary registration of 3D CT chest data to videobronchoscopy, but their results were limited [17]; (3) other researchers have proposed a fundamentally different approach whereby an extra electromagnetic sensor is attached to the bronchoscope tip — this approach also requires considerable extra hardware [5, 18, 19]; (4) Mori *et al.* registered videobronchoscopy images directly to rendered 3D CT images and also proposed including an electromagnetic sensor, but their efforts do not work interactively [20, 21].

Our efforts go beyond mere endoluminal renderings. Central to our work is the registration and fusion of radiologic CT image data and live endoscopic video. *We propose a method for performing this registration and fusion and describe a system that applies the method to the planning and guidance of live bronchoscopy.* Before the procedure, a 3D multi-detector CT (MDCT) chest scan is analyzed with the system. The physician constructs a multimedia case study that contains a list of predefined biopsy sites and a 3D airway path to each biopsy site. Next, the system is brought into the bronchoscopy laboratory and interfaced directly to the bronchoscope. The system then enables CT-video registration and fusion and provides live interactive bronchoscopic guidance to each biopsy site.

Before continuing, we give a general history of the major technologies involved in modern lung-cancer assessment: CT scanners, videobronchoscopes, and 3D computer-based visualization tools. Note that CT scanners have been in use for roughly 30 years and have many well accepted diagnostic uses. Also, new MDCT scanners readily give very large high-resolution 3D volumetric images of the chest [12, 14, 22] (Figure 1a). Similarly, bronchoscopes have been in regular clinical use for over 35 years. They also have many accepted diagnostic uses and provide high-resolution full-color real-time video of the interior wall structure of the human airways (Figure 1b) [2, 5]. Yet, CT scanners and videobronchoscopes have major limitations for assessing and staging lung cancer [22, 23]. FIGURE 1 HERE.

Modern MDCT scanners provide an enormous amount of high-resolution image data of the human chest. Unfortunately, physicians still primarily rely on either view panels to view a CT-scan film study or on computer workstations to do simple scrolling through CT slice data. Thus, the information contained in MDCT scans is woefully underutilized — this is a well-recognized problem in current radiology research [12,24]. Bronchoscopes have a related limitation in that they do not enable the physician to see beyond (extraluminally) the airway walls, nor do they enable the physician to see beyond the current position of the device; i.e., there is no look ahead [23].

Many 3D visualization techniques have been devised for more exhaustively viewing the information contained in 3D MDCT chest images. Examples of techniques are surface and volume rendering, multi-planar reformatted (MPR) slice viewing, projection imaging, thin-slab viewing, and endoluminal (virtual endoscopic) rendering [10, 12, 14, 23–26]. But, in reality, the visualization actually used in clinical practice is limited to previewing transverse-plane 2D slice images, occasional coronal and sagittal MPR sections, gray-scale windowing and thresholding to highlight structures of interest, and simple annotation and report generation. In addition, tools such as fluoroscopy and CT fluoroscopy are often available to the bronchoscopist, but they only provide either projection views or single 2D slice views and require extra radiation during a procedure [1, 27]. Thus, the clinical use of visualization tools for lung-cancer assessment still lags behind the developments made in the research laboratory.

Our efforts have attempted to close this gap. Our methods enable direct 3D CT-based procedure planning and provides direct 3D guidance during bronchoscopy. 3D CT-based information on biopsy sites is provided interactively as the physician moves the bronchoscope. Moreover, graphical information through a live fusion of the 3D CT data and bronchoscopic video is provided during a procedure. This information is coupled with a series of computer-graphics tools to give the physician a greatly augmented view of the patient's anatomy during a procedure. Section 2 of this paper overviews the basic system, while Section 3 describes the CT-video registration and fusion methods. Next, Section 4 provides a series of phantom, animal, and human results. Finally, Section 5 offers some concluding comments.

2 SYSTEM OVERVIEW

We first give an overview of the complete lung-cancer assessment system. The sections below overview the basic system hardware (Section 2.1), computer-based graphical user interface (Section 2.2), and basic system operation (Section 2.3).

2.1 System Hardware

Figure 2 gives a block diagram of the system's hardware. A standard Windows XP PC, equipped with a mid-range video card, serves as the main CPU unit. A Matrox Meteor-II frame grabber, driven by the MIL-Lite software library and plugged into one of the PC's PCI slots, acts as the interface to the live real-time video stream (30 frames per sec) from a bronchoscope's video output. The system's software architecture was initially conceived using the Unified Modeling Language (UML) and Rational Rose [28, 29]. All software is written in C++ and maintained in Visual Studio .NET 2003. The OpenGL and VTK (visualization toolkit) libraries are used for some of the visualization functions [30, 31].

FIGURE 2 HERE.

2.2 System Graphical User Interface

The system is used in two stages, per the basic lung-cancer assessment paradigm: *Stage-1 MDCT Assessment and Planning* followed by *Stage-2 Image-Guided Bronchoscopy.* The software is run through an integrated graphical user interface (GUI). Through the GUI, the user invokes interactive protocols for building a *case study* during Stage-1 MDCT Assessment and for performing live image-based guidance during Stage-2 Bronchoscopy. As described more below, the case study stores the following information for an incoming case: (1) segmented airway tree; (2) airway-tree endoluminal and extraluminal surface representations; (3) airway central axes (or centerlines); and (4) regions of interest (ROIs) signifying diagnostically important biopsy sites, such as lymph nodes or suspect cancer nodules.

The system has a wide range of interactive visualization tools. Figure 3 gives an example composite system view illustrating several of the available viewing tools, while other system examples appear later in Figures 4, 5, and 14. Many of these tools have been suggested by others in different contexts, but our system brings them together in a unique framework for lung-cancer assessment. The list below summarizes the available tools; the figure numbers in parentheses refer to examples of individual tool use:

1. Case Study — The user interacts through the case study to load image and centerline data, peruse the list of defined ROIs and associated surface data, capture 2D snapshots and AVI movies during Stage-1 MDCT Assessment and Stage-2 Bronchoscopy, set up the video source during bronchoscopy, and other functions. The case study serves as the general clearinghouse for interacting with various data elements. (See Figure 3.)

2. View Controls — Determines the mode for interacting with the various invoked visual tools. The user can select specific 3D sites, navigate forward or backward along a branch or complete

path defined within the airway-axes structure, or manually maneuver through the CT data. (See Figures 3 and 14.)

3. Projections — Coronal, sagittal, and transverse projections of the 3D CT data can be observed, with the precomputed central axes and ROIs superimposed. Weighted-sum projection, maximum-intensity projection (MIP), and other types of projections, computed within a defined 3D volume and window of intensities are available. A projection serves as a global viewer for interacting with the predefined central axes. (See Figures 3, 4, and 14).

4. Multiplanar reformatted (MPR) views [14] — In addition to standard transverse-section viewing, coronal and sagittal sections of the 3D CT volume can also be viewed. A flexible intensity-windowing facility exists, in addition to several standard windows used in pulmonary medicine. All views permit interactive 2D measurements of structures of interest. Further, both manual and semi-automatic 2D/3D methods are available for defining ROIs through these viewing tools [32]. (See Figures 3, 4, 5, and 14.)

5. Endoluminal Renderer — Endoluminal (virtual endoscopic) renderings of the airway interior can be displayed at 3D sites, using either volume or surface rendering [33]. (See Figure 4. This viewer is also a part of the Video Match tool as mentioned below.)

6. 3D Surface Renderer — A global 3D surface-rendered view of the segmented airway tree and predefined lymph node sites can be computed. This viewer also displays the extracted airway central axes. (See Figures 3, 4, 5, and 14.)

7. Shear-Warp Renderer — A fast interactive shear-warp renderer is available for global volume-rendered views of 3D MDCT data [34, 35].

8. Sliding Thin-slab (STS) Viewers — STS MIP, depth-weighted maximum, and other thin-slab views can be computed. Such views have been found to be particularly well suited for seeing interior soft tissue structures [26, 36, 37]. (See Figures 4, 5, and 14.)

9. Cross-Sectional Viewer — Small gray-scale MDCT sections, orthogonal to a 3D viewing site of interest, reveal local structure along an airway axis during navigation and interrogation [23, 33, 37–39].

10. Tube Viewer — Gray-scale cross-sections, interior renderings, and 3D topographic maps can be computed along mathematically unraveled (straightened) sections (tubes) of MDCT data along a 3D axis [23, 33, 40]. This gives a means for viewing data along a complete, and in general, tortuous airway path.

11. Plot Tool — A plot of geometric measurements along an airway (e.g., cross-sectional area, maximum airway diameter) can be displayed [23, 37–40]. The user can point to a selected site along this plot to see graphical manifestations of the MDCT data at this site.

5

12. Video Match Tool — This is the key tool used for CT-video registration and fusion and for enabling guidance during Stage-2 Bronchoscopy. More is said on this tool below. (See Figures 3, 5, and 14.)

Whether used during Stage-1 CT Assessment and Planning or Stage-2 Bronchooscopy, all system tools update continuously during interaction to provide a dynamic "augmented reality" view of the patient.

FIGURE 3 HERE.

2.3 Top-Level System Operation

Below, we summarize system usage during the two stages of operation. Stage 1 is only briefly highlighted in this paper, with other references giving more detail.

2.3.1 Stage 1: MDCT Assessment and Planning

Given the original 3D gray-level MDCT image, four processing steps are performed: (1) segment the airway tree; (2) compute the central axes of the extracted airways; (3) interactively identify the desired lymph-node biopsy sites as regions of interest (ROIs); (4) define the endoluminal and exterior surfaces of the segmented airway tree and the exterior surface of the ROIs for later rendering.

For airway tree segmentation, we have used methods based on 3D region growing and mathematical morphology [41]. For central-axes extraction, we have drawn upon techniques based on 3D thinning, B-spline analysis, and differential geometry [37, 39, 42]. For ROI definition, either direct manual slice tracing or more robust semi-automatic live-wire analysis have been used to identify region borders [32, 43, 44]. Surface data is generated using the well-known Marching Cubes algorithm built into the VTK package [30]. All Stage-1 methods have undergone considerable validation using real human data and are discussed in detail in previous publications.

After the analysis above is complete, the user previews the case information using various available visualization tools. Figure 4 gives an example during this step for an animal study. At the end of Stage-1 analysis, a case study exists that captures many data elements for follow-on report generation and a biopsy path plan to reach each ROI during subsequent Stage-2 Bronchoscopy.

FIGURE 4 HERE.

2.3.2 Stage 2: Image-Guided Bronchoscopy

Given the case study, a technician connects the bronchoscope's video stream to the computer system, as illustrated in Figure 2. The system's GUI is then set up in preparation for live bronchoscopic

guidance. Figure 5 gives a system view during Stage-2 bronchoscopy for same pig study as Figure 4, while Figure 14, discussed later, gives a view during a patient study.

Before proceeding, we must discuss the linkage between the two available data sources. As pointed out by Figure 1, the two fundamental data sources available to the system are the 3D MDCT chest image and the bronchoscope's video stream. Both sources capture different manifestations of structures inside the chest. The 3D MDCT image, being a digital replica of the chest, serves as a *Virtual World* version of the chest, while the bronchoscope video gives a *Real World* view of the interior of the lung airways.

Denote an endoscopic video frame as $I_V(x, y)$ and an MDCT-derived endoluminal rendering as $I_{CT}(x, y)$. As described further in Section 3, endoluminal renderings, computed from the 3D MDCT virtual-world data, also provide interior views of the lung airways. Both sources, I_V and I_{CT}, act as cameras observing the same space, namely the interior of the airway tree. Let the quantities, $I_V^\chi(x, y)$ and $I_{CT}^\chi(x, y)$, represent the bronchoscope and virtual CT views of 3D space at viewpoint $\chi = (X, Y, Z, \alpha, \beta, \gamma)$, where (X, Y, Z) represents the camera's 3D global spatial position in World coordinates and (α, β, γ) are angles specifying camera orientation about the camera's focal point.

The critical processing step during live guidance is the registration of the MDCT and video data sources. Let $I_V^F(x, y)$ represent a fixed target video frame and let $I_{CT}^{\chi_i}(x, y)$ denote an initial MDCT-based endoluminal rendering at initial viewpoint χ_i. During registration, the following optimization is run to search for the optimal viewpoint χ_o:

$$\chi_o = \arg \left\{ \max_{\chi \in N_{\chi_i}} \left[S_{NMI} \left(I_{CT}^\chi(x, y), I_V^F(x, y) \right) \right] \right\} \tag{1}$$

$I_{CT}^{\chi_o}(x, y)$ is the endoluminal rendering best matching the fixed video frame $I_V^F(x, y)$. In (1), N_{χ_i} is the search neighborhood about χ_i and S_{NMI} represents the normalized mutual information (NMI) between $I_{CT}^\chi(x, y)$ and $I_V^F(x, y)$ [45]. Section 3 gives more detail on the optimization (1).

With this introduction, we now describe the basic Stage-2 operation of the system. To guide the physician to each lymph-node ROI site, the following steps are taken:

1. Select the case study's precomputed path that was found during Stage 1 to lead to the lymph-node site.

2. Select an initial site along the path that serves as a target for the physician to move the bronchoscope. For this site, compute the MDCT-based endoluminal rendering $I_{CT}^{\chi_i}(x, y)$, where χ_i is the initial viewpoint as represented in the selected 3D site's data structure. Generally, the site is selected by picking a point on a 2D coronal projection of the 3D MDCT data set and associated computed central axes. The point is picked on the highlighted path

activated in step 1. As a rule for bronchoscopy, the first selected site is generally within the trachea near the main carina.

3. The physician maneuvers the bronchoscope "close" to the active site. This gives a fixed target video frame $I_V^F(x, y)$.

4. The computer dynamically registers the MDCT world, starting with view $I_{CT}^{\chi_i}(x, y)$, to the fixed target video frame $I_V^F(x, y)$, per the optimization (1). The result of this registration results in view $I_{CT}^{\chi_o}(x, y)$ at the optimal viewpoint χ_o best matching the target video frame. In this way the 3D MDCT "virtual world" is brought into synchrony with the "real" world as captured by the bronchoscopic video.

5. Select another site along the path toward the lymph node. This gives a new target MDCT-based endoluminal rendering $I_{CT}^{\chi_i}(x, y)$.

6. The physician again moves the bronchoscope close to the new $I_{CT}^{\chi_i}(x, y)$ and the registration process of step 4 is repeated.

7. Steps 5 and 6 are repeated until the physician believes that the bronchoscope is sufficiently close to the site of interest.

During bronchoscopy, active system tools, such as the Coronal Projection and 3D Surface tools, continuously update to give visual progress down the path toward the ROI. Notably, the Video Match Tool continuously depicts the incoming video, registered MDCT-based endoluminal rendering, and a data-fused version of the MDCT data and video. The Video Match tool also gives various distance measurements, indicating how close the bronchoscope is to a target ROI. Figures 3 and 5 (and other later figures) give example system views during bronchoscopy.
FIGURE 5 HERE.

3 CT-VIDEO REGISTRATION AND FUSION

Details on the internal registration and fusion processes are given below. In particular, Section 3.1 describes the physical models underlying I_{CT} and I_V and the basic registration operation, while Section 3.2 details the optimization methods. Finally, Section 3.3 describes how fusion is accomplished between the CT and video data. For this paper, we follow the notational conventions of [46].

3.1 Source Modeling and the Registration Method

As mentioned earlier, the endoscopic video $I_V(x, y)$ and endoluminal renderings $I_{CT}(x, y)$ act as cameras observing the same 3D space. To facilitate one-to-one pixel-based (x, y) registration be-

tween these two cameras, we first measure off-line (before a procedure) the focal length and field-of-view dimensions of the bronchoscope. These quantities are easily measured, per [46,47]. The measured quantities are then used to compute endoluminal renderings $I_{CT}(x, y)$ for the virtual-world camera.

For our work, we use the luminance (gray-scale) component of the bronchoscope's video. Okatani and Deguchi have shown that the illuminated endoluminal airway walls can be modeled as a Lambertian surface and that the brightness of an airway surface point $\mathbf{p}$ can be specified by [48]

$$I(\mathbf{p}) = \sigma \frac{L \cos \theta_s}{\pi R^2} \tag{2}$$

where L is the intensity of the bronchoscope's light source, θ_s is the angle between the light source and $\mathbf{p}$'s surface normal, R is the distance from the light source to $\mathbf{p}$, and σ is a proportionality factor that takes into account airway-surface albedo and the bronchoscope's device characteristics [46]. The final 2D point $I_V(x, y)$ then results from a standard 3D-to-2D transformation of $I(\mathbf{p})$.

For computing the endoluminal renderings, the value $I_{CT}^{\chi}(x, y)$ of a particular screen point (x, y), which corresponds to an observed surface point $\mathbf{p}$, abides by a model similar to the endoscope Lambertian shading model of (2):

$$I_{CT}^{\chi}(x, y) = \frac{(\cos \phi_{\mathbf{p}})^{1/2} \cos \theta_s}{(1 + .0025R^2)} + L_a \tag{3}$$

Eq. (3) differs from (2) in three important ways:

1. An ambient light factor L_a is included to approximate the indirect lighting.

2. The denominator arising from the range attenuation term is forced to stay > 0, which is again required for real computer-based rendering. R is derived from a known range map (derived from the previously computed airway-tree surface data) and measured in mm for (3).

3. The bronchoscope's light source is in fact close to the surfaces it is illuminating. Hence, the light source in fact changes in illumination intensity as one moves off the axis of the light source (same as the camera axis). The attenuation factor $(\cos \phi_{\mathbf{p}})^{1/2}$, where $\phi_{\mathbf{p}}$ is the angle between the camera axis and the vector pointing toward point $\mathbf{p}$, represents this illumination change.

Eq. (3) is easily implemented by the OpenGL command `gllightf()` and contrast scaled for an eight-bit gray-scale display [31]. Note that (2) is a model for a video frame $I_V(x, y)$ (we do not have control over this), while (3) is our controllable implementation of the CT-based camera producing frames $I_{CT}(x, y)$. Extensive results for controlled and real tests, given in [46], have validated the efficacy of these models.

Equation (1) is the central optimization performed during CT-video registration. The discussion below gives more detail on (1). S_{NMI} is defined as [45, 46]:

$$S_{NMI}(I_V, I_{CT}) = \frac{h(V) + h(CT)}{h(V, CT)}$$

where $h(V)$ and $h(CT)$ are entropy-like quantities for I_V and I_{CT}, and $h(V, CT)$ is a joint entropy between I_V and I_{CT}; $h(V)$ is given by

$$h(V) = -\frac{1}{M^2} \sum_{k=0}^{M-1} \sum_{l=0}^{M-1} w_k w_l p_{V,CT}(k, l) \log p_V(k) \tag{4}$$

where $p_V(k)$ is the probability density function (pdf) for the pixel gray-level values contained in I_V, $p_{V,CT}(k, l)$ is the joint gray-scale histogram between I_V and I_{CT}, and the w_k (and w_l) are weights. The pdf $p_V(k)$ is estimated as the normalized histogram of I_V, per:

$$p_V(k) = \frac{1}{N_x N_y} \sum_{x=1}^{N_x} \sum_{y=1}^{N_y} \delta(k - I_V(x, y)), \tag{5}$$

while the quantity $p_{V,CT}(k, l)$ is the 2D joint intensity pdf between the two images I_{CT} and I_V defined as

$$p_{V,CT}(k, l) = \frac{1}{N_x N_y} \sum_{x=1}^{N_x} \sum_{y=1}^{N_y} \delta(k - I_V(x, y)) \delta(l - I_{CT}(x, y)). \tag{6}$$

In (5-6), $\delta(k)$ is the discrete Dirac delta function such that $\delta(k) = 1$ for $k = 0$ and $\delta(k) = 0$ for all other k. $I_V(x, y)$ and $I_{CT}(x, y)$ denote the grayscale values of pixel (x, y) in the two $N_x \times N_y$ images, where the grayscale values range from 0 to $M - 1$. The quantities $h(CT)$ and $h(V, CT)$ have definitions similar to (4). Finally, the weights are set to favor the more informative darker pixels:

$$w_k = (M - k)/M, \quad k = 0, 1, \ldots, M - 1.$$

As observed by Bricault, the darker areas in I_V and I_{CT} give "more useful information," as they correspond to significant features such as upcoming airway bifurcations and other airway-wall deviations, whereas the bright "bland" areas offer little useful information [17]. Reference [46] gives further discussion on the quantities above.

Figure 6 gives an example of the quantities used in the optimization. Despite the differences in the image pdf's, the similarities between the two data sources are apparent. This similarity (mutual information) is maximized by the optimization. This results in an approximately diagonal joint density. The diagonal characteristic implies that the intensity values of the two matching views, $I_V^F(x, y)$ and $I_{CT}^{\chi_o}(x, y)$, lie along a line of the form

$$I_V^F(x, y) \approx I_{CT}^{\chi_o}(x, y) + b$$

for most pixel locations (x, y) in the two frames; the quantity $b > 0$ represents the ambient intensity bias in the video frame, which is generally brighter on average than the endoluminal rendering.

FIGURE 6 HERE.

3.2 Optimization

We applied three optimization techniques for solving the registration problem: (a) brute-force steepest ascent [49, 50]; (b) simplex [51, 52]; and (c) simulated annealing [53]. In our early efforts, we found that the steepest-ascent approach often converges to a proper optimum, but it is also vulnerable to unwanted local optima [49, 50]. Thus, we have abandoned it as a viable alternative.

For the simplex algorithm (Figure 7), an initial N-dimensional simplex ($N = 6$), defined by seven vertices, χ_i, $i = 0, 2, \ldots, N$, is first defined. The vertices signify candidate optimal viewpoints. During algorithm iteration, χ_{min}, the current "worst" vertex having lowest S_{NMI} measure, is reflected by a factor -1 across the face of the simplex to give a new candidate vertex χ^*. If χ^* improves upon S_{max}, the current maximum S_{NMI} measure found, then the algorithm tests to see if a factor -2 reflection of χ_{min}, giving χ^{**}, helps. If reflection does not improve the search, then the worst vertex is contracted a factor $\frac{1}{2}$ inward toward the face of the simplex, giving candidate vertex χ^{***}. If this doesn't help, then all vertices are contracted a factor $\frac{1}{2}$ toward the current optimal vertex. The iteration continues, with the simplex gradually converging toward and shrinking around the final optimum.

FIGURE 7 HERE.

For the simulated annealing method (Figure 8), $U(0, T)$ is a uniform random variable distributed between 0 and T, where T is temperature. The standard deviation of $U(0, T)$ is proportional to T by the definition of the uniform distribution. Random values are also subtracted from S_{NMI} at reflections, expansions, and contractions to allow the solution to jump out of local minima. The temperature is defined as the standard deviation of the added random variation. The temperature is high at the start of the algorithm to create more randomness. It is lowered according to the annealing schedule, so that towards the end of the search it behaves like the straightforward simplex method. During iteration through a temperature step, the solution can stray from the optimal. Thus, the best value found during all operations of a step is saved and used as the starting value for iteration with the next temperature step.

FIGURE 8 HERE.

Both the simplex and simulated-annealing algorithms always gave satisfactory maxima, provided that the viewpoint χ_i of the initial input CT rendering $I_{CT}^{\chi_i}(x, y)$ started sufficiently close to the optimal viewpoint χ_o. Reference [46, 50] give extensive tests on the sensitivity of the op-

timization methods to starting point χ_i. It was found that individual spatial position values, X, Y, or Z, could vary $\geq \pm 6$ mm and viewpoint angles, α, β, or γ, could vary $\geq \pm 20^o$ from χ_o and result in proper convergence. Given that a typical airway has a diameter on the order of 10mm, these values imply great flexibility in starting point. Our tests indicate that the steepest ascent method required 8.91 sec per optimization, simplex 23.16 sec, and simulated annealing 24.04 sec on a dual-processor 933MHz PC. We in general used the simplex method in our tests.

3.3 CT-Video Fusion

Once the optimization (1) is complete, $I_{CT}^{\chi_o}(x, y)$ corresponds to the CT-based endoluminal rendering best matching the given real bronchoscopic video frame $I_V(x, y)$. In addition, χ_o signifies the viewpoint to use in 3D space for computing system views derived from the 3D MDCT data and for performing data fusion between the CT data and video stream.

As mentioned in Section 2.3.2, the Video Match tool provides the fused information. The data-fused view merges the video and MDCT-based ROI, much as was done by Grimson *et al.* in a different image-guided surgery application [54]. Referring to Figure 3, the Video Match tool's middle view depicts an example $I_{CT}^{\chi_o}(x, y)$. This view shows the target ROI and path from the point of view of the 3D CT data registered to the current bronchoscope position. The right panel of the Video Match tool then shows $I_V^F(x, y)$ with the CT-derived ROI fused onto the view. In this way, the physician has a virtual target mapped onto the live video.

Computation of the fused view requires two important processing steps. First, during bronchoscopy, the bronchoscopic video stream undergoes continuous real-time distortion correction so that it matches the field of view (FOV) of a "virtual world" camera inside the 3D MDCT data. As an example, Figure 1b depicts a raw bronchoscopic video frame before distortion correction, while the left panels of the Video Match tools illustrated in this paper (e.g., Figure 3) depict corrected views. Reference [47] discusses this distortion correction procedure in detail. With the FOVs of the two cameras matched, a direct point-by-point correspondence now exists between a video view $I_V(x, y)$ and CT-derived view $I_{CT}(x, y)$. This enables proper registration (1) and subsequent fusion of the CT-derived ROI with the video frame.

The second important processing step toward computing a fused view involves how the view is actually computed. With the FOVs matched between the virtual CT world and the real bronchoscopic video world, it is a straightforward matter to map the ROI surface into the 2D space observed by the video source; this involves a simple projection operation. So as not to obscure the underlying video, the ROI is rendered transparently onto the video frame.

We emphasize that for our application the real target is never visible in the video, as the lymph

nodes are situated outside the airway interior. By fusing the CT information with the live video information, the system is able to provide live guidance information on extraluminal biopsy sites that would not otherwise be visible.

In addition to view fusion, several quantitative distances are computed on the fly during the procedure and presented by the Video Match tool. Referring to the Video Match tool in Figure 3, "Min Airway to ROI Surface" represents the minimum distance of *any* of the visible ROI points in the center panel to the airway surface. "Dist to ROI Center" represents the distance from the FOV center to the ROI's centroid. "Airway Surface" gives the distance of the airway location pointed to by the cursor (arrow in center panel) to the airway-wall surface, while "Airway to ROI Surface" gives the distance of the airway-wall location pointed to by the cursor to the ROI surface (these two distances appear in the footer of the Video Match tool). Therefore, the sum of these two distances gives the total distance of the cursor's airway location to the ROI surface.

4 RESULTS

This section gives results for phantom, animal, and human studies.

We first tested the biopsy accuracy of our system for a controlled phantom experiment. The phantom used was a translucent rubber airway-tree replica, with six 1.4mm-diameter platinum beads glued to its exterior surface. The beads served as ROI "biopsy sites." An MDCT scan was made for the phantom, and Stage-1 MDCT Assessment and Planning operations were performed. Two physicians used our system during bronchoscopy to "biopsy" each bead. During guided bronchoscopy, the computer display included the 3D Surface tool, Coronal Projection, Transverse Slicer, Coronal Slab, and Video Match Tool. The procedure of Section 2.3.2 was used to guide the physician to each bead. The physician stuck a biopsy needle into the phantom's rubber wall as the best biopsy point. Figure 9 shows a set of views from the Video Match tool when a physician is contemplating a biopsy. A measurement was then taken with a caliper as the distance between the metal bead and the line perpendicular to the needle direction. Figure 10 shows that the average biopsy error for the two physicians was 1.97mm. Typical chest diagnostic sites have a diameter $\geq$10mm; hence, these results are very encouraging. A follow-up test with the same phantom involving six physicians gave an average error of 1.57mm [46]. This compares very favorably to another trial involving the same six physicians performing the biopsies using the standard unguided CT-film approach (average error = 5.53mm). In fact, this test revealed that the six physicians not only all improved in performance, but they also became nearly indistinguishable in performance. This implies that the difference in physician skill level does not affect biopsy performance.

FIGURES 9-10 HERE.

We next performed five pig studies. These studies enabled us to test the system's feasibility, safety, and effectiveness during controlled in vivo circumstances, without the pressure of worrying about procedural errors such as puncturing major vessels. They also motivated tests of system reliability and new system enhancements.

Each pig was administered general anesthesia, transferred supine onto the CT scanner table, and placed on a PC pressure and ECC monitor. An Imatron EBCT scanner was used for the first three studies, while a Marconi Mx8000 MDCT scanner was used for the final two studies. A lung volume controller stabilized the chest volume at functional residual capacity during a CT scan [55]. In all studies, we first performed a 3D CT scan of the animal, applied Stage-1 MDCT Analysis (e.g., Figure 4), and then defined several "virtual" ROIs within the CT data. These steps took approximately five to ten minutes. Then, during Stage-2 Bronchoscopy, we used the system to guide the physician to each virtual ROI (e.g, Figure 5). Upon reaching a biopsy site, the physician then either deposited a dye marker or a metallic dart at the site. Figure 11 illustrates a system view after a dart was deposited at one virtual site. The animal then underwent a second CT scan. Next, the initial CT scan (with virtual ROIs) and the second CT scan (with dye markers or darts) were compared. Figure 12 shows comparison 3D CT views that indicate the ROI target region and placed platinum dart. In this experiment the ROIs were below the airway wall, but the dart could only penetrate the surface, making the final dart position slightly above the initial ROI. Figure 12 show that the dart for the ROI seemed to be placed well near the target, indicating proper guidance to this region.

FIGURES 11-12

The animal studies, done over a two-year period, helped to introduce additions and improvements to the system, such as the distance calculations now present in the Video Match tool [56]. Also, software bugs, such as a memory leak that caused the system to freeze after 5-10 continuous minutes of live operation, were fixed. For the final animal study performed with the MDCT scanner, we placed six ROIs within the two lungs, spaced at locations near generation-2 and generation-5 airways. For these studies, we achieved the following results: average distance from the ROI center: 4.95mm; average distance from the ROI: 2.37mm.

The errors achieved by the animal studies are again small. As another point, the animal studies also gave us the opportunity to test the overall safety of the system. In particular, we wanted to see if the system provided misleading information such as guidance to major arteries that should not be punctured. We observed no such events during these studies. We did observe, however, that for one peripheral biopsy site, the 6mm-diameter Olympus bronchoscope used for the studies could not be physically manipulated within the airway near the site. Hence, the biopsy could not

be done. But, this is a limitation of the device, not our system. Current ultrathin bronchoscopes (diameters on the order of 2.8mm) offer promise for navigating through small airways [57–59].

After establishing general reliability and safety through the animal studies, we next performed a pilot study of the system under real clinical circumstances. Figure 13 presents information on eleven human lung-cancer patients enrolled in the study. All patients had known mediastinal adenopathy and were enrolled under informed consent. For each patient, a 3D MDCT chest scan was done using a Philips 4-detector Mx8000 MDCT scanner. Patients held their breath for 20 sec. during a scan. We then went through Stage-1 MDCT Assessment and Planning operations to arrive at a computer-based case study and all preplanned ROI biopsy sites.

In the bronchoscopy laboratory, the system was then interfaced to the bronchoscope, per Figure 2. For each planned site, the physician received continuous image guidance data and performed the appropriate biopsy. For immediate confirmation, cytology was done after each biopsy. Three different medical-school staff physicians, typically assisted by fellows-in-training, performed the procedures.

Case RJ represented the first "dry run" system test. The goal of case RJ was to gain confidence with the experimental apparatus in a real clinical scenario. The system was applied successfully in all tests. For case PK, the physician erroneously defined a blood vessel segment as the ROI. This was not a malfunction of the system, as the available system viewing tools clearly were able to show that this site was a blood vessel. In fact, the system actually guided the physician "successfully" to this ROI during the procedure. As with any new device, this test did show that caution and proper training are necessary to use the system properly. Figure 14 presents a captured computer screen for case HW, where the live bronchoscopy needle appears in the view. As a result of this procedure, the nodal region samples showed cancer consistent with the patient's known previous renal cell information.

FIGURES 13-14 HERE.

5   DISCUSSION

Several issues warrant discussion regarding the proposed image-guided bronchoscopy system. First, during a bronchoscopy, the physician must cooperate in that the bronchoscope cannot be moved too quickly. This requirement adds no undue burden, as the physician generally tends to hover over sites of interest within the airways. The quickest movements occur when the physician pulls the bronchoscope away from a site after finishing a biopsy. Bear in mind that the distances that the bronchoscope is moved is measured in mm and cm — small movements are the rule. A second issue involves the differing chest volumes during MDCT scanning (patient holds breath and the

lungs are near full inflation) and during bronchoscopy (patient is doing low-level tidal breathing and the lungs stay largely deflated). We have found through laboratory and animal studies that this phenomenon has no impact on the guidance [46]. This is apparently true, because the airways are largely rigid cartilaginous structures and the working environment during CT-video registration is very small (on the order of a few cm^3). A final issue involves events occurring during bronchoscopy, such as patient coughs, water bubbles, airway-wall obscurations (the bronchoscope tip goes against an airway wall obscuring the view). We have considered some preliminary efforts to detect such events [60].

Other emerging tools could conceivably improve the overall efficacy of our system. Endobronchial ultrasound (EBUS) has the ability to detect a desired ROI locally during bronchoscopy [61]. EBUS could synergistically complement our system's guidance, but further miniaturization of the EBUS device would be necessary for them to be feasible at peripheral sites. Positron emission tomography (PET) and the recent innovation of combined PET-CT scanners adds yet another tool for procedure planning [61–63]. While researchers assert that PET can specifically identify positive cancer sites, its inherent low resolution limits its diagnostic capability for small lesions. In addition, direct in vivo diagnostic intervention with bronchoscopy would still be required to confirm a diagnosis.

The phantom, animal, and human studies done to date have helped confirm the safety and minimal risk in using the system. There is essentially no risk, as the physician can merely ignore the computer and follow only the bronchoscopic video as ever. Note that the current system already fits readily into the clinical work flow, with technicians performing nearly all tasks. During Stage-1 MDCT analysis, the physician's only task is to point out ROIs, while during Stage-2 bronchoscopy, the physician does nothing extra except look at the system's computer monitor.

Other researchers have demonstrated recently that VB-based guidance during bronchoscopy can provide the necessary means for successful peripheral nodule biopsy [64, 65]. But more definitive 3D MDCT-based path planning would offer a more exhaustive and straightforward means for preplanning appropriate endobronchial routes for maneuvering the bronchoscope through the complex airway tree and would specify the final biopsy site (often invisible in current practice) definitively [66]. Finally, recent developments in real-time continuous CT-video registration during bronchoscopy could potentially further improve image-based guidance [67, 68].

6 ACKNOWLEDGMENTS

References

[1] A. D. Sihoe and A. P. Yim, "Lung cancer staging," *J. Surgical Research*, vol. 117, no. 1, pp. 92–106, Mar. 2004.

[2] K. P. Wang and A. Mehta, eds., *Flexible Bronchoscopy*. Cambridge, MA: Blackwell Science, 1995.

[3] H. P. McAdams, P. C. Goodman, and P. Kussin, "Virtual bronchoscopy for directing transbronchial needle aspiration of hilar and mediastinal lymph nodes: a pilot study," *Am. J. Roentgenology*, vol. 170, pp. 1361–1364, May 1998.

[4] K. Hopper, T. Lucas, K. Gleeson, J. Stauffer, R. Bascom, D. Mauger, and R. Mahraj, "Transbronchial biopsy with virtual CT bronchoscopy and nodal highlighting," *Radiology*, vol. 221, no. 2, pp. 531–536, Nov. 2001.

[5] F. Herth, R. Eberhardt, and A. Ernst, "The future of bronchoscopy in diagnosing, staging, and treatment of lung cancer," *Respiration*, vol. 73, pp. 399–409, 2006.

[6] D. Osborne, P. Vock, J. Godwin, and P. Silverman, "CT identification of bronchopulmonary segments: 50 normal subjects," *AJR*, vol. 142, pp. 47–52, 1984.

[7] M. Y. Dolina, L. V. Buyantseva, S. A. Merritt, L. Rai, K. Lu, C. R. Cope, W. E. Higgins, R. Mahraj, M. Tucakovic, and R. Bascom, "Comparison of transverse chest CT images and a virtual navigation endoluminal image for bronchoscopy path selection to endoluminal pulmonary nodules," in *Proceedings of the American Thoracic Society*, p. A541, April 2006.

[8] H. Minami, Y. Ando, F. Nomura, S. Sakai, and K. Shimokata, "Interbronchoscopist variability in the diagnosis of lung cancer by flexible bronchoscopy," *Chest*, vol. 105, no. 2, pp. 1658–1662, June 1994.

[9] D. J. Vining, K. Liu, R. H. Choplin, and E. F. Haponik, "Relationships of virtual reality endobronchial simulations to actual bronchoscopic findings (preliminary report)," *Chest*, vol. 109, no. 2, pp. 549–553, 1996.

[10] G. D. Rubin, C. F. Beaulieu, V. Argiro, H. Ringl, A. M. Norbash, J. F. Feller, M. D. Dake, S. Napel, R. B. Jeffrey, and S. Napel, "Perspective volume rendering of CT and MR images: applications for endoscopic imaging," *Radiology*, vol. 199, no. 2, pp. 321–330, May 1996.

[11] E. F. Haponik, S. L. Aquino, and D. J. Vining, "Virtual bronchoscopy," *Clinics in Chest Med.*, vol. 20, no. 1, pp. 201–217, March 1999.

[12] P. M. Boiselle, K. F. Reynolds, and A. Ernst, "Multiplanar and three-dimensional imaging of the central airways with multidetector CT," *Am. J. Roentgenology*, vol. 179, pp. 301–308, Aug. 2002.

[13] P. Turcza and M. Duplaga, "Navigation systems based on registration of endoscopic and CT-derived virtual images for bronchofiberoscopic procedures," in *Studies in Health Technology and Informatics: Transformation of Health Care with Information Technologies*, M. Duplaga, K. Zielinski, and D. Ingram, eds., vol. 105, pp. 253–263, IOS Press, Sept. 2004.

[14] N. C. Dalrymple, S. R. Prasad, M. W. Freckleton, and K. N. Chintapalli, "Introduction to the language of three-dimensional imaging with multidetector CT," *Radiographics*, vol. 25, no. 5, pp. 1409–1428, Sept.-Oct. 2005.

[15] W. E. Lorensen, F. A. Jolesz, and R. Kikinis, "The exploration of cross-sectional data with a virtual endoscope," *Interactive Technology and the New Health Paradigm*, pp. 221–230, Jan. 1995.

[16] P. Rogalla, J. Van Scheltinga, and B. Hamm, *Virtual Endoscopy and Related 3D Techniques*. Berlin: Springer-Verlag, 2002.

[17] I. Bricault, G. Ferretti, and P. Cinquin, "Registration of real and CT-derived virtual bronchoscopic images to assist transbronchial biopsy," *IEEE Transactions on Medical Imaging*, vol. 17, no. 5, pp. 703–714, Oct. 1998.

[18] Y. Schwarz, A. C. Mehta, A. Ernst, F. Herth, A. Engel, D. Besser, and H. D. Becker, "Elecromagnetic navigation during flexible bronchoscopy," *Respiration*, vol. 70, no. 5, pp. 515–522, Sept.-Oct. 2003.

[19] T. R. Gildea, P. J. Mazzone, D. Karnak, M. Mezlane, and A. C. Mehta, "Electromagnetic navigation diagnostic bronchoscopy," *Am. J. Respir. Crit. Care Med.*, vol. 174, pp. 982–989, 2006.

[20] K. Mori, D. Deguchi, J. Sugiyama, Y. Suenaga, J. Toriwaki, C. R. Maurer, H. Takabatake, and H. Natori, "Tracking of bronchoscope using epipolar geometry analysis and intensity-based image registration of real and virtual endoscopic images," *Medical Image Analysis*, vol. 6, pp. 321–336, 2002.

[21] K. Mori, D. Deguchi, K. Akiyama, T. Kitasaka, C. R. Maurer, Y. Suenaga, H. Takabatake, M. Mori, and H. Natori, "Hybrid bronchoscope tracking using a magnetic tracking sensor and image registration," in *Medical Image Computing and Computer Assisted Intervention 2005*, J. Duncan and G. Gerig, eds., vol. LNCS 3750, pp. 543–550, 2005.

[22] E. A. Kazerooni, "High resolution CT of the lungs," *Am. J. Roentgenology*, no. 3, pp. 501–519, Sept. 2001.

[23] W. E. Higgins, K. Ramaswamy, R. Swift, G. McLennan, and E. A. Hoffman, "Virtual bronchoscopy for 3D pulmonary image assessment: State of the art and future needs," *Radiographics*, vol. 18, no. 3, pp. 761–778, May-June 1998.

[24] G. Ferretti, I. Bricault, and M. Coulomb, "Virtual tools for imaging of the thorax," *Eur. Respir. J.*, vol. 18, pp. 381–392, 2001.

[25] R. M. Summers, "Navigational aids for real-time virtual bronchoscopy," *Am. J. Roentgen.*, vol. 168, pp. 1165–1170, May 1997.

[26] J. Z. Turlington and W. E. Higgins, "New techniques for efficient sliding thin-slab volume visualization," *IEEE Transactions in Medical Imaging*, vol. 20, no. 8, pp. 823–835, Aug. 2001.

[27] C. S. White, E. A. Weiner, P. Patel, and E. J. Britt, "Transbronchial needle aspiration: guidance with CT fluoroscopy," *Chest*, vol. 118, no. 6, pp. 1630–1638, Dec. 2000.

[28] A. Sherbondy, "PC-based system for virtual endoscopy," Master's thesis, The Pennsylvania State University, University Park, PA., 2001.

[29] J. Rumbaugh, *The Unified Modeling Language Reference Manual*. Boston: Addison-Wesley, 2005.

[30] W. Schroeder, K. Martin, and B. Lorensen, *The Visualization Toolkit, 2nd. Ed.* Upper Saddle River, New Jersey: Prentice Hall, 1998.

[31] R. S. Wright, Jr., and B. Lipchak, *OpenGL Super Bible, 3rd. Ed.* SAMS Publishing, 2005.

[32] K. Lu and W. E. Higgins, "Improved 3D live-wire method with application to 3D CT chest image analysis," in *SPIE Medical Imaging 2006: Image Processing*, J. M. Reinhardt and J. P. W. Pluim, eds., vol. 6144, pp. 189–203, 2006.

[33] K. Ramaswamy and W. E. Higgins, "Interactive dynamic navigation for virtual endoscopy," *Computers in Biology and Medicine*, vol. 29, no. 5, pp. 303–331, Sept.-Oct. 1999.

[34] P. Lacroute and M. Levoy, "Fast volume rendering using a shear-warp factorization of the viewing transformation," *SIGGRAPH 94, Comp. Graphics Proc., Annual Conf Series*, pp. 451–458, 1994.

[35] W. E. Higgins, L. Rai, S. A. Merritt, K. Lu, N. T. Linger, and K. C. Yu, "3D image fusion and guidance for computer-assisted bronchoscopy," in *SPIE Optics East: Three-Dimensional TV, Video, and Display IV*, B. Javidi, F. Okano, and J.-Y. Son, eds., vol. 6016, pp. 86–100, Nov. 2005.

[36] S. Napel, G. D. Rubin, and R. B. Jeffrey, "STS-MIP, a new reconstruction technique for CT of the chest," *Journal of Computer Assisted Tomography*, vol. 17, no. 5, pp. 832–838, 1993.

[37] R. D. Swift, A. P. Kiraly, A. J. Sherbondy, A. L. Austin, E. A. Hoffman, G. McLennan, and W. E. Higgins, "Automatic axes-generation for virtual bronchoscopic assessment of major airway obstructions," *Computerized Medical Imaging and Graphics*, vol. 26, no. 2, pp. 103–118, March-April 2002.

[38] K. Ramaswamy and W. E. Higgins, "Endoscopic exploration and measurement in 3D radiological images," *SPIE Med. Imaging 1996: Image Processing*, vol. 2710, Newport Beach, CA, pp. 511–523, Feb. 1996.

[39] A. P. Kiraly, J. P. Helferty, E. A. Hoffman, G. McLennan, and W. E. Higgins, "3D path planning for virtual bronchoscopy," *IEEE Trans. Medical Imaging*, vol. 23, no. 11, pp. 1365–1379, November 2004.

[40] A. P. Kiraly, J. M. Reinhardt, E. A. Hoffman, G. McLennan, and W. E. Higgins, "Virtual bronchoscopy for quantitative airway analysis," in *SPIE Medical Imaging 2005: Physiology, Function, and Structure from Medical Images*, vol. 5746, A. Amini, and A. Manduca, eds. pp. 369-383, 2005.

[41] A. P. Kiraly, W. E. Higgins, E. A. Hoffman, G. McLennan, and J. M. Reinhardt, "3D human airway segmentation methods for virtual bronchoscopy," *Academic Radiology*, vol. 9, no. 10, pp. 1153–1168, Oct. 2002.

[42] K. C. Yu, E. L. Ritman, and W. E. Higgins, "3D model-based vasculature analysis using differential geometry," in *IEEE Int. Symp. on Biomedical Imaging*, pp. 177–180, Arlington, VA, 15-18 April 2004.

[43] A. J. Sherbondy, A. P. Kiraly, A. L. Austin, J. P. Helferty, S. Wan, J. Z. Turlington, E. A. Hoffman, G. McLennan, and W. E. Higgins, "Virtual bronchoscopic approach for combining 3D CT and endoscopic video," *SPIE Medical Imaging 2000: Physiology and Function from Multidimensional Images, A. Clough and C.T. Chen, eds.*, vol. 3978, pp. 104–116, Feb. 12-17, 2000.

[44] K. Lu and W. E. Higgins, "Interactive segmentation based on the live wire for 3D CT chest image analysis," *Int. J. Comput. Assisted Radiol. Surgery*, 2007. in press.

[45] C. Studholme, D. L. G. Hill, and D. J. Hawkes, "An overlap invariant entropy measure of 3D medical image alignment," *Pattern Recognition*, vol. 32, no. 1, pp. 71–86, Jan. 1999.

[46] J. P. Helferty, A. J. Sherbondy, A. P. Kiraly, and W. E. Higgins, "Computer-based system for the virtual-bronchoscopic guidance of bronchoscopy," *Computer Vision and Image Understanding*, vol. 108, no. 1-2, pp. 171–187, Oct.-Nov. 2007.

[47] J. P. Helferty, C. Zhang, G. McLennan, and W. E. Higgins, "Videoendoscopic distortion correction and its application to virtual guidance of endoscopy," *IEEE Trans. Med. Imaging*, vol. 20, no. 7, pp. 605–617, July 2001.

[48] T. Okatani and K. Deguchi, "Shape reconstruction from an endoscope image by shape from from shading technique for a point light source at the projection center," *Computer Vision and Image Understanding*, vol. 66, no. 2, pp. 119–131, May 1997.

[49] J. P. Helferty and W. E. Higgins, "Technique for registering 3D virtual CT images to endoscopic video," *IEEE Int. Conf. Image Processing*, vol. II, pp. 893–896, Oct. 7-10 2001.

[50] J. P. Helferty, E. A. Hoffman, G. McLennan, and W. E. Higgins, "CT-video registration accuracy for virtual guidance of bronchoscopy," in *SPIE Medical Imaging 2004: Physiology, Function, and Structure from Medical Images,*, vol. 5369, A. Amini, and A. Manduca, eds. pp. 150-164, 2004.

[51] J. A. Nelder and R. Mead, "A simplex method for function optimization," *The Computer Journal*, vol. 7, pp. 308–313, 1965.

[52] W. H. Press, *Numerical Recipes in C: the Art of Scientific Computing*. Cambridge University Press, 1994.

[53] N. Ritter, R. Owens, J. Cooper, R. H. Eikelboom, and P. P. Van Saarloos, "Registration of stereo and temporal images of the retina," *IEEE Trans. on Medical Imaging*, vol. 18, no. 5, pp. 404–418, May 1999.

[54] W. E. Grimson, G. J. Ettinger, S. J. White, T. Lozano-Perez, W. E. Wells III, and R. Kikinis, "An automatic registration method for frameless stereotaxy, image guided surgery, and enhanced reality visualization," *IEEE Transactions on Medical Imaging*, vol. 15, no. 2, pp. 129–140, Apr. 1996.

[55] B. Q. Tran, J. K. Tajik, R. A. Chiplunkar, and E. A. Hoffman, "Lung volume control for quantitative x-ray CT," *Annals of Biomed. Engin.*, vol. 24, no. Supplement 1, pp. S–66, 1996.

[56] J. P. Helferty, A. J. Sherbondy, A. P. Kiraly, J. Z. Turlington, E. A. Hoffman, G. McLennan, and W. E. Higgins, "Experiments in virtual-endoscopic guidance of bronchoscopy," *SPIE Medical Imaging 2001: Physiology and Function from Multidimensional Images,*, vol. 4321, pp. 111–121, 2001. C. T. Chen and A. V. Clough (ed.).

[57] F. Asano, Y. Matsuno, T. Matsushita, H. Kondo, Y. Saito, A. Seko, and Y. Ishihara, "Transbronchial Diagnosis of A Pulmonary Peripheral Small Lesion Using an Ultrathin Bronchoscope with Virtual Bronchoscopic Navigation," *Bronchology*, vol. 9, no. 2, pp. 108–111, Apr. 2002.

[58] F. Asano, J. Shindoh, K. Shigemitsu, K. Miya, T. Abe, M. Horiba, and Y. Ishihara, "Ultrathin bronchoscopic barium marking with virtual bronchoscopic navigation for fluoroscopy-assisted thoracoscopic surgery," *Chest*, vol. 126, no. 5, pp. 1687–1693, Nov. 2004.

[59] N. Shinagawa, K. Yamazaki, Y. Onodera, K. Miyasaka, E. Kikuchi, H. Dosaka-Akita, and M. Nishimura, "CT-guided transbronchial biopsy using an ultrathin bronchoscope with virtual bronchoscopic navigation," *Chest*, vol. 125, no. 3, pp. 1138–1143, Mar. 2004.

[60] W. E. Higgins, J. P. Helferty, and D. R. Padfield, "Integrated bronchoscopic video tracking and 3D CT registration for virtual bronchoscopy," *SPIE Medical Imaging 2003: Physiology and Function: Methods, Systems and Applications,*, vol. 5031, pp. 80–89, 2003. A.V. Clough and A.A. Amini (ed.).

[61] K. Yasufuku, T. Nakajima, K. Motoori, Y. Sekine, K. Shibuya, K. Hiroshima, and T. Fujisawa, "Comparison of endobronchial ultrasound, positron emission tomography, and CT for lymph node staging of lung cancer," *Chest*, vol. 130, no. 3, pp. 710–718, Sept. 2006.

[62] P. Boiselle, E. Patz, D. Vining, R. Weissleder, J. Shepard, and T. McLoud, "Imaging of mediastinal lymph nodes: CT, MR, and FDG PET," *Radiographics*, vol. 18, no. 5, pp. 1061–1070, Sept.-Oct. 1998.

[63] A. S. Bryant, R. J. Cerfolio, K. M. Klemm, and B. Ohja, "Maximum standard uptake value of mediastinal lymph nodes on integrated FDG-PET-CT predicts pathology in patients with non-small cell lung cancer," *Ann. Thorac. Surg.*, vol. 82, no. 2, pp. 424–429, Aug. 2006.

[64] F. Asano, Y. Matsuno, N. Shinigawa, K. Yamazaki, T. Suzuki, T. Ishida, and H. Moriya, "A virtual bronchoscopic navigation system for pulmonary peripheral lesions," *Chest*, vol. 130, no. 2, pp. 559–565, Aug. 2006.

[65] N. Shinagawa, K. Yamazaki, Y. Onodera, F. Asano, T. Ishida, H. Moriya, and M. Nishimura, "Virtual bronchoscopic navigation system shortens the examination time — feasibility study of virtual bronchoscopic navigation system," *Lung Cancer*, vol. 56, no. 2, pp. 201–206, May 2007.

[66] J. D. Gibbs and W. E. Higgins, "3D path planning and extension for endoscopic guidance," in *SPIE Medical Imaging 2007: Visualization and Image-Guided Procedures*, K. R. Cleary and M. I. Miga, eds., vol. 6509, pp. 65091K–65091 – 65091K–65013, 2007.

[67] S. A. Merritt, L. Rai, and W. E. Higgins, "Real-time CT-video registration for continuous endoscopic guidance," in *SPIE Medical Imaging 2006: Physiology, Function, and Structure from Medical Images*, A. Manduca and A. A. Amini, eds., vol. 6143, pp. 370–384, 2006.

[68] S. A. Merritt, L. Rai, J. D. Gibbs, K. C. Yu, and W. E. Higgins, "Method for continuous guidance of endoscopy," in *SPIE Medical Imaging 2007: Physiology, Function, and Structure from Medical Images*, A. Manduca and X. P. Hu, eds., vol. 6511, pp. 6511D0–1 — 6511D0–12, 2007.
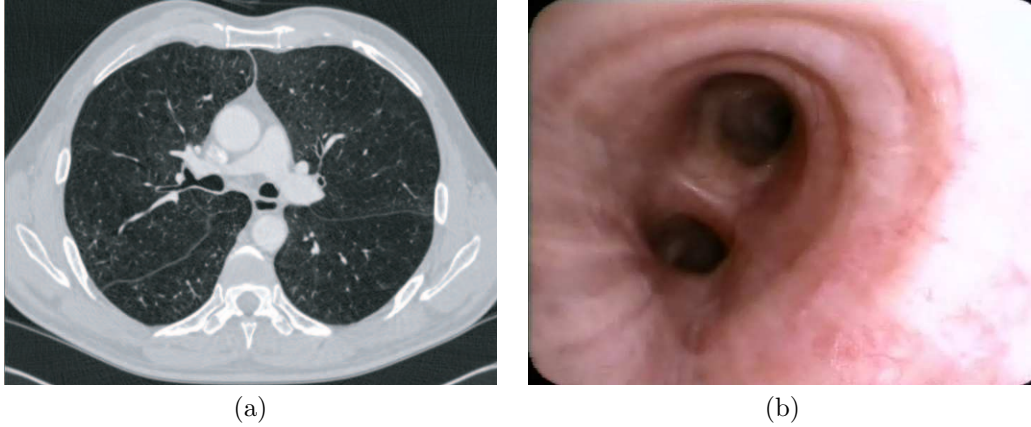
(a)   (b)

Figure 1: Complementary data sources for patient 21405-3a, used for lung-cancer assessment. (a) 2D Transverse slice 304 from a $512\times512\times704$ MDCT human thoracic image (Siemens Sensation-16 16-detector MDCT scanner, $\Delta x = \Delta y = 0.67$mm and $\Delta z = 0.5$mm; (b) bronchoscope video frame from a Pentax EB1570 videobronchoscope (frame rate: 30 frames/sec.).
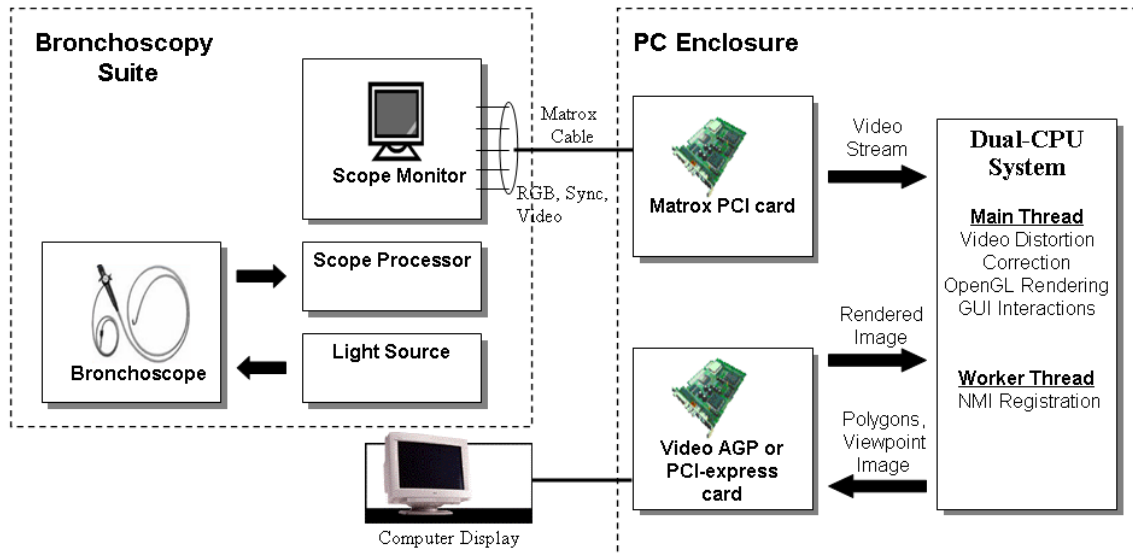
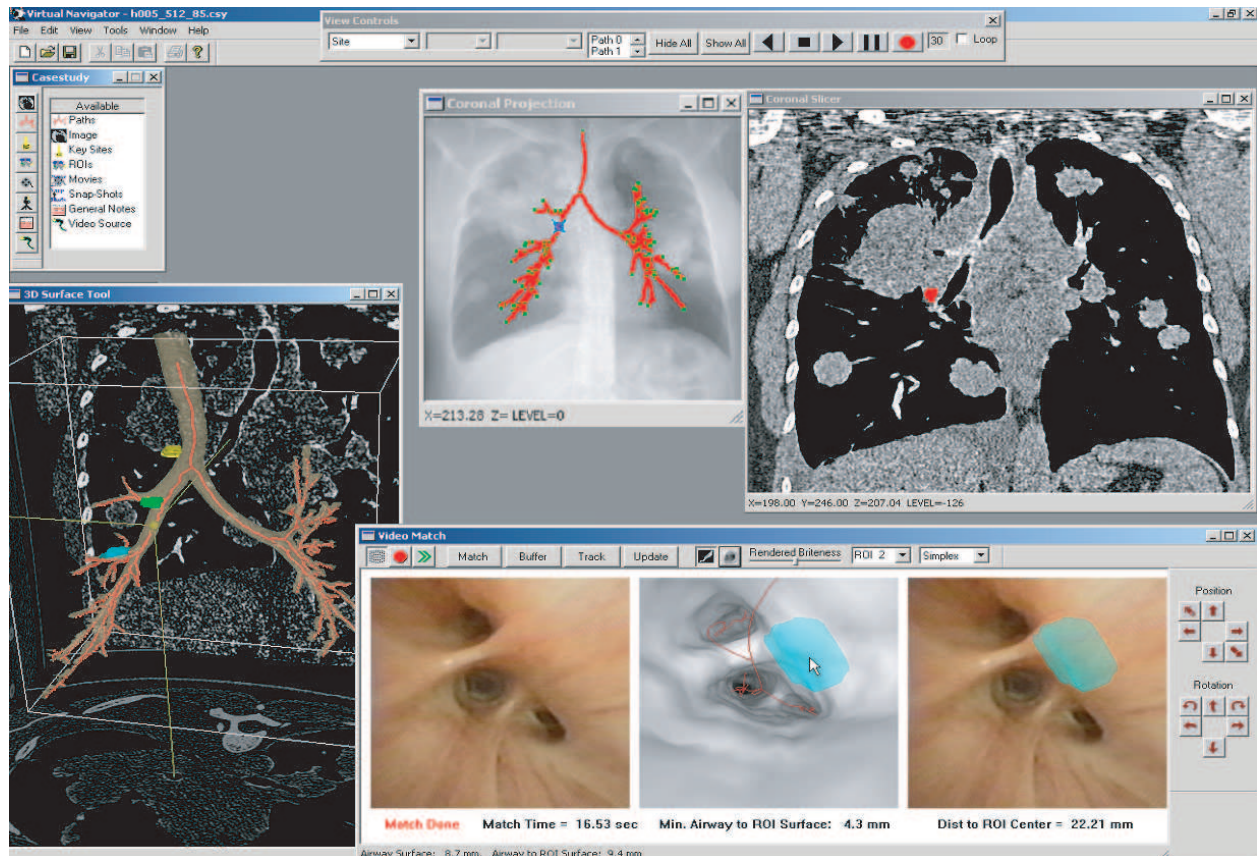

Figure 2: Block diagram of system hardware.

Figure 3: System snapshot for human case UF (see Figure 13). Upper left panel shows the Case Study, a repository for case data. Top center bar shows the View Controls, used for navigation. 3D Surface Tool (lower left) shows segmented airway tree and precomputed red centerlines. Yellow ball indicates the location of the current viewing site in the virtual 3D CT world. Yellow, green, and blue regions are lymph nodes manually predefined. Top center view shows coronal maximum-intensity projection of data, with red centerlines; blue dot is current site. Top right view shows a coronal MPR slice with a region cross-section (red). Bottom right view shows the Video Match tool, which gives the result of NMI registration of the 3D CT virtual endoluminal view. The Video Match tool's left panel depicts the live bronchoscopic video, the middle panel gives the registered endoluminal rendering, and the right panel depicts a fusion of the blue lymph-node ROI (from the MDCT data) onto the video frame.
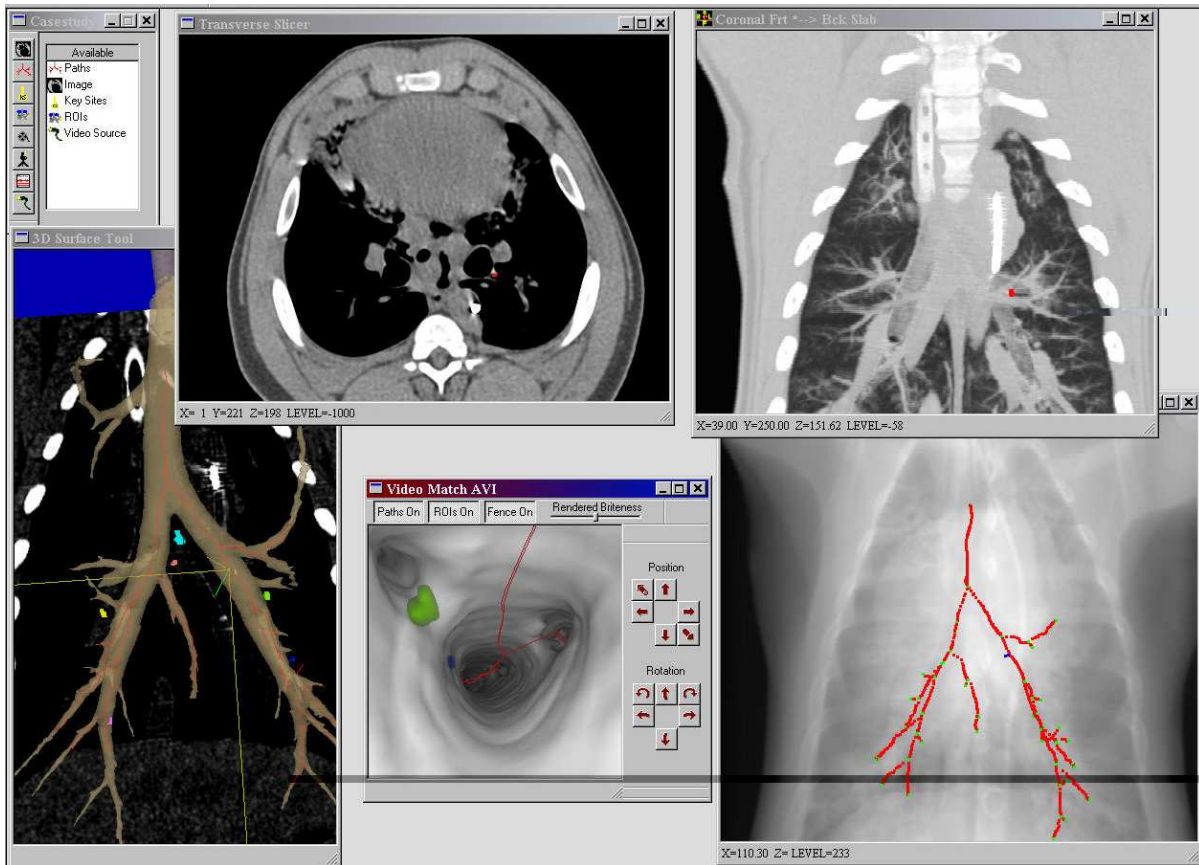
Figure 4: Example system lay-out during Stage-1 CT assessment for an animal study. Upper left view illustrates the case study. Lower left view shows a 3D Surface Tool view of the segmented airway tree, extracted axes (red lines), five ROIs of various colors (small blobs external to the rendered tree), and a coronal slice passing through the selected 3D site; the selected site appears as a small green needle intersecting by yellow orthogonal reference axes. Top left view is a coronal depth-weighted maximum thin-slab; the red dot indicates the current 3D site. Lower center view is an endoluminal rendering of the selected 3D site, where the red lines are the extracted airway axes again, the green blob is the green ROI also seen in the 3D Surface tool; note that transparency is used for this rendering, so that the green ROI becomes visible. The lower right dialog is a coronal maximum-intensity projection (MIP) of the 3D MDCT data set, and the red lines again indicate the extracted central axes.
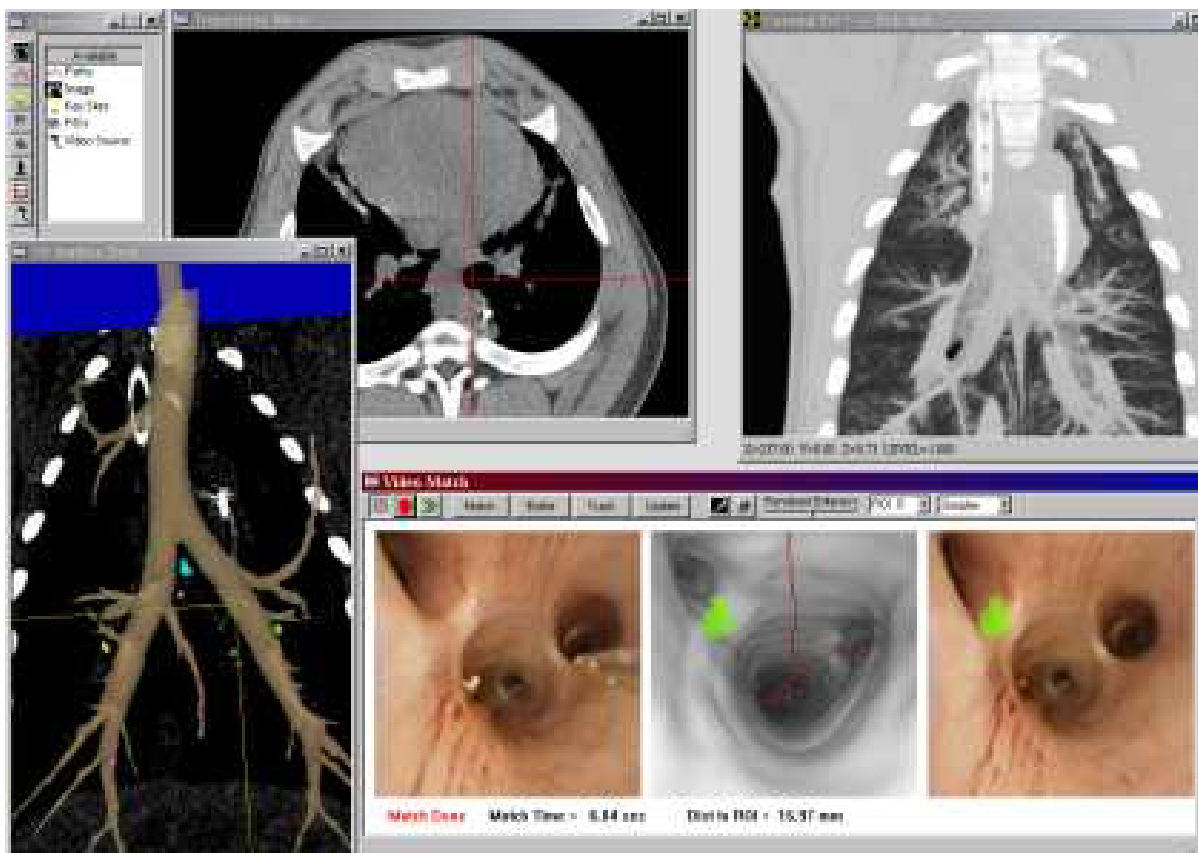
23

Figure 5: Example system lay-out during Stage-2 Image-Guided Bronchoscopy for an animal study. Near same 3D site as in Figure 4. Transverse slice view, Coronal Thin-Slab view, and 3D Surface Tool are similar to those shown in Figure 4. The lower right dialog depicts the Video Match tool during a procedure at the chosen 3D site: the left view shows the live video (notice the presence of the biopsy needle); the center view depicts the registered endoluminal rendering, which shows the previous extracted central axes (serve as guidance paths) and the current target ROI (green blob); the right view depicts a fusion of the CT-based virtual ROI onto the registered video frame.
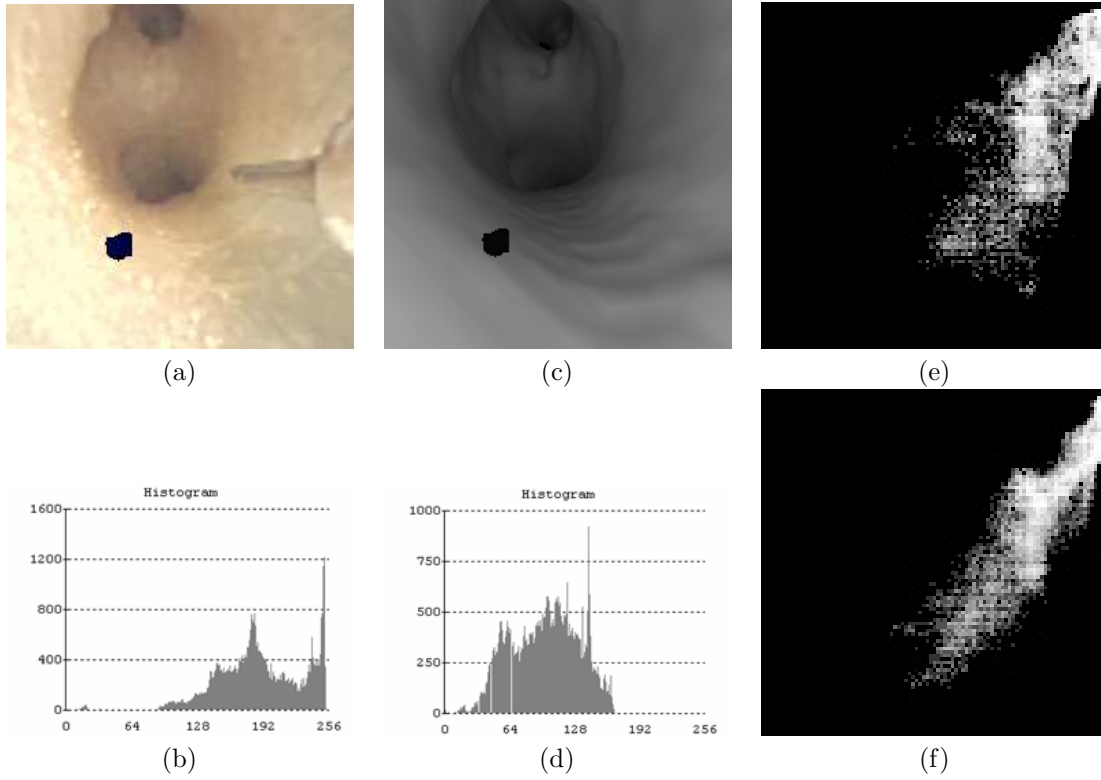
Figure 6: CT-Video registration example: (a) video frame $I_V(x,y)$ (needle and ROI [black region] present); (b) $p_V(k)$ for $I_V(x,y)$; (c) registered CT-based rendering $I_{CT}(x,y)$; (d) $p_{CT}(k)$ for $I_{CT}(x,y)$; (e) joint density $p_{V,CT}(k,l)$ before registration, where the horizontal axis represent the gray-scale value of the video and the vertical axis is the gray-scale value of the endoluminal rendering; (f) optimal joint density $p_{V,CT}(k,l)$ after registration. The video frame is brighter on the average than the CT rendering, as is clear from the pdf's — this accounts for the intensity shift in the joint density.

Calculate vertices of initial simplex (N=6):

$\quad \chi_0 = \{X, Y, Z, \alpha, \beta, \gamma\}$ (initial viewpoint), $\chi_1 = \{X+\Delta X, Y, Z, \alpha, \beta, \gamma\}, \ldots, \chi_N = \{X, Y, Z, \alpha, \beta, \gamma+\Delta\gamma\}$

$i = 0$

Do

$\quad$ Compute $S_{NMI}(\chi_i), \quad i = 0, 1, \ldots, N$

$\quad$ Note the best and worst vertices and associated NMI measures: $\chi_{min}, \chi_{max}, S_{min}, S_{max}$

$\quad$ Get reflection of χ_{min} across face of simplex: $\chi^* = (\frac{2}{N} \sum_{\chi_i \neq \chi_{min}} \chi_i) - \chi_{min}$

$\quad$ **If** $(S_{NMI}(\chi^*) > S_{max})$

$\quad\quad$ Get 2× reflection of χ_{min} across face of simplex: $\chi^{**} = (\frac{3}{N} \sum_{\chi_i \neq \chi_{min}} \chi_i) - 2\chi_{min}$

$\quad\quad$ **If** $(S_{NMI}(\chi^{**}) > S_{max})$ $\quad \chi_{max} = \chi^{**}$

$\quad\quad$ **Else** $\quad \chi_{max} = \chi^*$

$\quad$ **Else**

$\quad\quad$ Contract χ_{min} $\frac{1}{2}$ distance toward face of simplex: $\chi^{***} = (\frac{1}{2N} \sum_{\chi_i \neq \chi_{min}} \chi_i) + \frac{1}{2}\chi_{min}$

$\quad\quad$ **If** $(S_{NMI}(\chi^{***}) > S_{min})$ $\quad \chi_{min} = \chi^{***}$

$\quad\quad$ **Else** $\quad$ contract all vertices $\chi_i \neq \chi_{max}$ $\frac{1}{2}$ distance toward χ_{max}: $\chi_i = \frac{1}{2}(\chi_i + \chi_{max})$

$\quad i = i + 1$

While $\{(S_{max} - S_{min}) > S_{tol}$ and $i < I_{max}\}$

Figure 7: Simplex algorithm. Error tolerance factor S_{tol} and maximum number of iterations run I_{max} are user selected parameters. For this paper, $S_{tol} = 0.002$ and $I_{max} = 200$.

Calculate vertices, $\chi_0, \chi_1, \ldots, \chi_N$, of initial simplex, where χ_0 is the starting viewpoint
Set initial temperature $T = T_0$
$i = 0$
Do
    Compute $S_{NMI}(\chi_i) + U(0, T), \quad i = 0, 1, \ldots, N$
    Note the best and worst vertices and associated NMI measures: χ_{min}, χ_{max}, S_{min}, S_{max}
    Get reflection of χ_{min} across face of simplex to get χ^*
    If $((S_{NMI}(\chi^*) - U(0, T)) > S_{max})$
        Get 2× reflection of χ_{min} across face of simplex to get χ^{**}
        If $((S_{NMI}(\chi^{**}) - U(0, T)) > S_{max}) \quad \chi_{max} = \chi^{**}$
        Else $\chi_{max} = \chi^*$
    Else
        Contract χ_{min} $\frac{1}{2}$ distance toward face of simplex to get χ^{***}
        If $((S_{NMI}(\chi^{***}) - U(0, T)) > S_{min}) \quad \chi_{min} = \chi^{***}$
        Else   contract all vertices $\chi_i \neq \chi_{max}$ $\frac{1}{2}$ distance toward χ_{max}
    $i = i + 1$
    $T = T - \Delta T$
While $\{ (T > 0)$ and $((S_{max} - S_{min}) > S_{tol})$ and $(i < I_{max}) \}$

Figure 8: Simulated annealing algorithm. This algorithm expands the simplex algorithm of Fig. 7 to include random perturbations at each iteration. All other aspects of the method are the same as the simplex method. Error tolerance factor S_{tol}, maximum number of iterations run I_{max}, T_0 and ΔT are user-selected parameters. For this paper, $S_{tol} = 0.002$, $I_{max} = 200$, $T_0 = 0.005$, and $\Delta T = 0.001$.
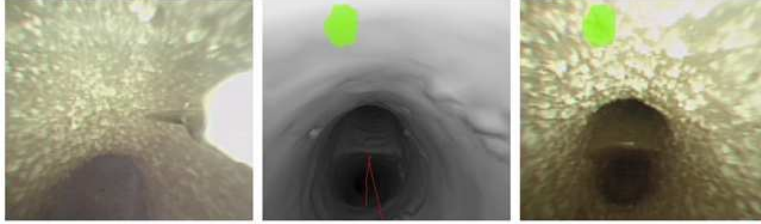

Figure 9: Video Match tool during live image-guided phantom "biopsy." The complete system view is similar to that shown in Figure 3. Left panel: current live video with biopsy needle visible. Middle: NMI-registered endoluminal view with ROI in green. Right: frozen reference registered video view with ROI fused onto view.

Subject	Distance (mm)	Std. Dev.
Physician #1, trial 1	2.18	1.09
Physician #1, trial 2	1.73	0.98
Physician #2	2.01	0.89
Average	1.97	0.94

Figure 10: Phantom biopsy results. Two physicians used the proposed system to "biopsy" a rubber human airway-tree phantom enhanced with six platinum beads serving as ROIs. A $453 \times 155 \times 160$ MDCT scan (Marconi Mx8000 4-detector scanner; $\Delta x = \Delta y = 0.35mm$ and $\Delta z = 1.5mm$) was made. "Distance" gives the average biopsy error over measurements made for five beads. "Std Dev" is the standard deviation of the measurements. "Average" represents the average biopsy results over the three trials.
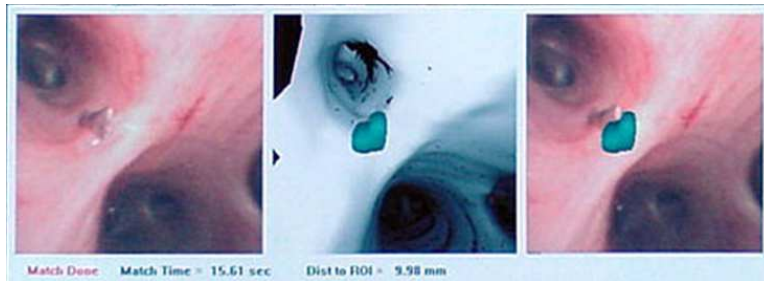
Figure 11: Video Match tool view during live bronchoscopy for an animal study. The view shows results after a biopsy dart was placed successfully at an ROI site. The live video view on the left shows the dart, the middle view shows the registered endoluminal view with blue ROI just before the dart is placed, and the right frozen video depicts the dart and superimposed ROI. MDCT scan parameters: 512×512×440 3D MDCT volume dimensions, scanned on Marconi Mx8000 MDCT scanner, sampling increments are $\Delta x = \Delta y = 0.44$mm and $\Delta z = 0.60$, ventilation of animal was controlled during the scan.

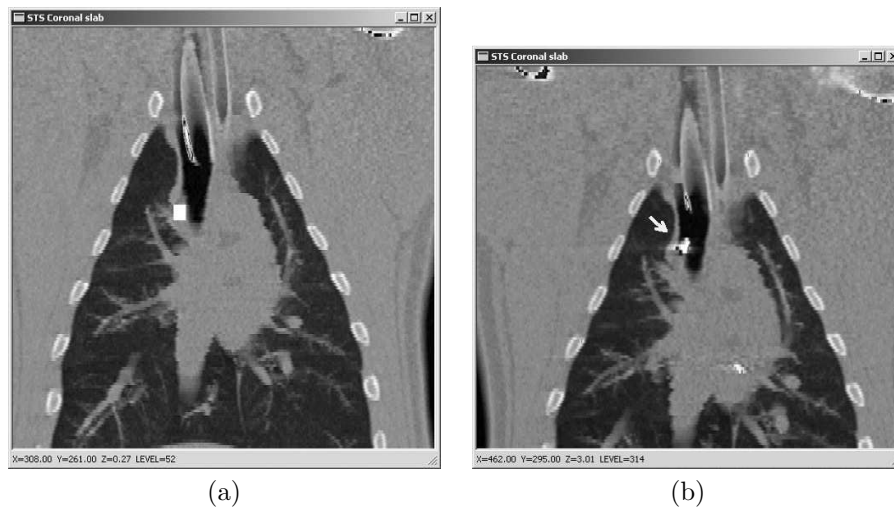(a)   (b)

Figure 12: Depth-weighted maximum coronal slab views (depth of vision = 15) [26]) comparing the CT scan before bronchoscopy and a second CT scan after guided bronchoscopy with platinum darts deposited. (a) View depicting a target ROI in "before" scan. (b) View depicting dart location in "after" scan, showing that the dart is slightly above the ROI position (arrow shows dart position), indicating a good location. Imatron EBCT scan parameters: 512×512×140 image dimensions, $\Delta x = \Delta y$ =0.41mm, Δz =1.5mm.

27

Subject	Age	Male/Female	Description	Results
RJ	86	M	Mediastinal nodes	First live dry run. No biopsies attempted, so guided bronchoscopy was not done.
DC	49	M	Right upper lobe inflammatory mass with mediastinal nodes.	Needle aspiration showed normal lymph node material.
UF	51	F	Multiple pulmonary nodules with mediastinal adenopathy.	Needle aspiration showed cancer.
PK	74	F	Interstitial lung disease with mediastinal adenopathy.	Needle aspiration showed blood only (wrong region outlined).
HW	72	M	Right lower lobe nodule with subcarinal nodes.	Needle aspiration showed renal cell cancer.
AD	79	M	Pharyngeal carcinoma with mediastinal nodes.	Needle aspiration showed normal lymphoid material.
LH	55	F	Head and neck cancer with mediastinal lymphadenopathy.	Needle aspiration showed normal lymphoid material.
MM	52	F	Left hilar mass of lymph nodes. Lung mass with histoplasmosis.	Needle aspiration of nodes shows normal lymphoid material.
DW	57	M	Squamous cell cancer of larynx. Right paratracheal nodes.	Mediastinal aspiration biopsy with no tumor or lymphocytes seen.
MB	54	M	Paratracheal lymphadenopathy	Mediastinal aspiration biopsy with no tumor or lymphocytes seen.
FT	41	F	Mediastinal mass	Mediastinal mass aspiration biopsy with non-necrotizing granulomas.

Figure 13: Table of cases and procedural results for a human lung-cancer patient pilot study.
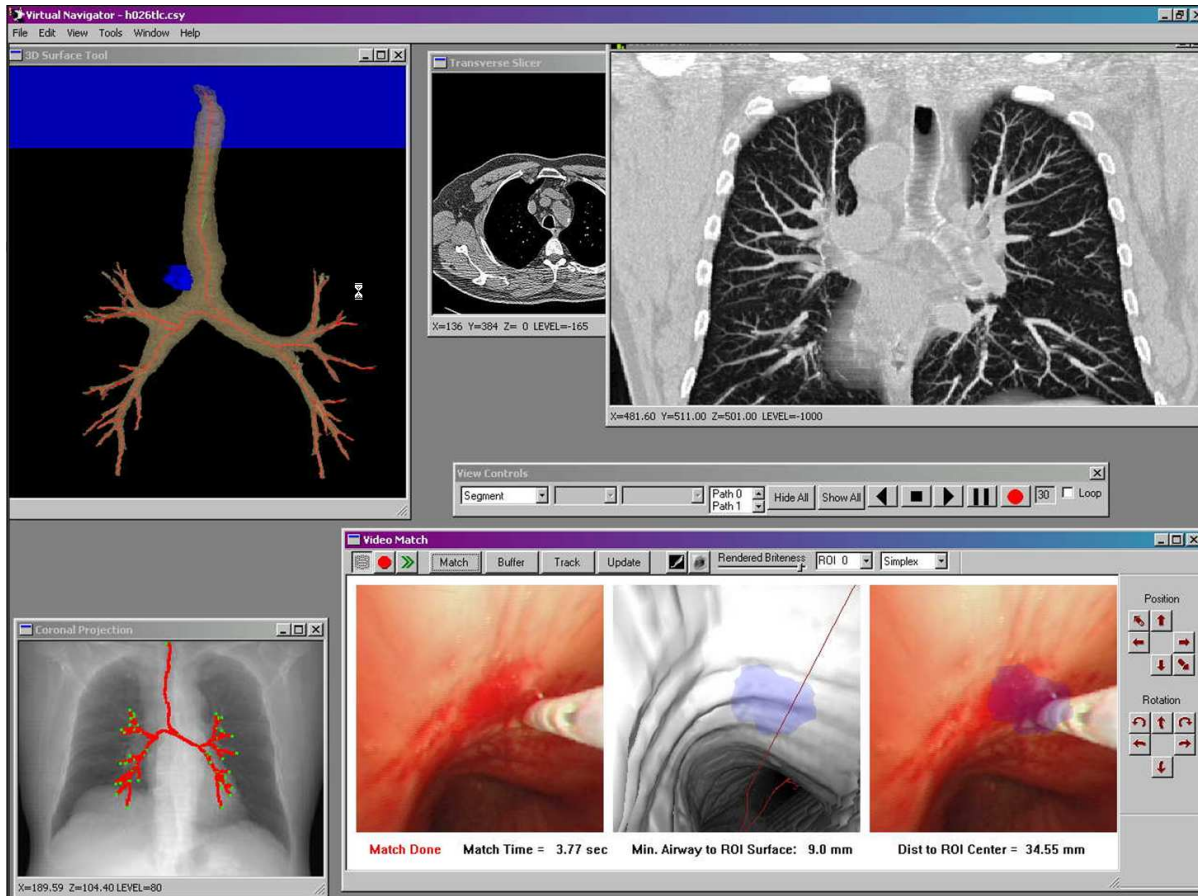
Figure 14: System snapshot during a live mediastinal lymph node biopsy for human case HW. Patient has a right lower-lobe nodule, with sub-carinal nodes. A right paratracheal node was predefined manually as an ROI. Lower right gives results for live CT-Video registration (Video Match Tool). Left panel is current live video frame. Center panel is matching 3D CT endoluminal view after NMI registration; purple region is the ROI (red line is centerline being followed to site). Right panel gives ROI rendered onto video frame, with *real aspiration needle visible.* Top right view shows 3D Surface Tool with rendered segmented airway tree and red automatically defined centerlines. Lower left view gives Coronal Maximum-Intensity Projection with centerlines. Upper right view giving a depth-weighted Coronal Slab vividly shows anatomy in the vicinity of the ROI.

SUMMARY

Interventional biopsy of the central-chest lymph nodes is an important step for staging lung cancer. Trans-bronchial needle aspiration (TBNA) is often used to sample lymph nodes for pathology. To perform TBNA, the physician first visually assesses a patient's computed tomography (CT) scan to identify suspect lymph-node sites. Later, during subsequent live bronchoscopy, the physician guides the bronchoscope to each desired lymph-node site. Unfortunately, the physician has no link between the 3D CT image data and the live video stream provided during bronchoscopy. In addition, these data sources differ greatly in what they physically give. This makes it difficult for the physician to translate a CT-based procedure plan to the video domain of the bronchoscope. Thus, the physician must essentially perform biopsy blindly, and the skill levels between different physicians differ greatly. We describe an approach that enables synergistic fusion between the 3D CT data and the bronchoscopic video. Both the integrated planning and guidance system and the internal CT-video registration and fusion methods are described. Given models for the CT and video sources, we use an optimization method based on normalized mutual information to register the 3D CT data to the live bronchoscopic video source. This then enables computer-graphics-based fusion of CT information with the video. During bronchoscopy, 3D CT-based information on biopsy sites is provided interactively as the physician moves the bronchoscope. Moreover, graphical information through a live fusion of the 3D CT data and bronchoscopic video is provided during the procedure. This information is coupled with a series of computer-graphics tools to give the physician a greatly augmented reality of the patient's interior anatomy during a procedure. A series of controlled phantom and animal studies and studies with human lung-cancer patients illustrate the efficacy of the system.